Density gradient calculation in a class of multiphase lattice Boltzmann models

Rongzong Huang,[1,2,3,*] Huiying Wu,[2,†] and Nikolaus A. Adams[3,‡]

[1]*School of Energy Science and Engineering, Central South University, 410083 Changsha, China*

[2]*School of Mechanical Engineering, Shanghai Jiao Tong University, 200240 Shanghai, China*

[3]*Institute of Aerodynamics and Fluid Mechanics, Technical University of Munich, 85748 Garching, Germany*

(Received 7 March 2019; revised manuscript received 8 September 2019; published 21 October 2019)

The multiphase lattice Boltzmann (LB) models based on pairwise interactions show great potential for simulating multiphase flows due to the conceptual and computational simplicity. Although the dynamics of multiphase flows are reproduced by the pairwise interaction force, the gradient of density (or effective density, i.e., pseudopotential) is implicitly involved in these models via the specialized forcing scheme or the consistent scheme for ε^3-order term. This work focuses on the calculation of density gradient in this class of multiphase LB models. Theoretical analyses are first carried out to reveal the involvement and calculation of density gradient. On the basis of a low Mach number approximation, an improved scheme is then proposed to calculate the density gradient for the recent LB model with self-tuning equation of state. Analytical and numerical calculations show that the improved scheme is more accurate and can help to reduce the numerical error when the reduced temperature is relatively low.

DOI: 10.1103/PhysRevE.100.043306

I. INTRODUCTION

Multiphase flows are widely encountered in daily life and have important applications in engineering, like phase-change heat sink and digital microfluidics [1,2]. The dynamics of multiphase flows, such as phase transition and separation, interface breakup and coalescence, nonzero surface tension, etc., are quite varied and complex from the macroscopic viewpoint. Physically speaking, all the associated dynamics are the natural consequences of the underlying molecular interactions at the microscopic level, which can be approximately modeled by the Lennard-Jones potential consisting of a short-range repulsive core and a long-range attractive tail [3]. As a mesoscopic numerical method that originates from the lattice gas automata and can be derived from the kinetic theory in an *a priori* manner [4–6], the lattice Boltzmann (LB) method shows potential for incorporating the microscopic interactions and thus for modeling multiphase flows without resorting to interface capturing or tracking techniques [7–10].

The applications of LB method to multiphase flows emerged at the early stage of its development [7–9]. Various LB models have been proposed for multiphase flows, which can be generally categorized into the color-gradient LB model [7,11], the Shan-Chen LB model [8,12], the free-energy LB model [9,13], and the phase-field LB model [14,15]. Among these models, the Shan-Chen LB model, which is originally proposed by Shan and Chen [8] and also termed the pseudopotential LB model, is the simplest one in both concept and computation. In this model, pairwise interactions are introduced to mimic the underlying molecular interactions responsible for multiphase flows. Because of this clear physical picture, the pseudopotential LB model has attracted significant attention since its first development, and the practical applications of this model are quite wide [16–18]. In addition to the above models, some kinetic-theory-based LB models for multiphase flows have also be developed in an *a priori* manner [3,10,19]. Though with a solid basis in kinetic theory, these models are rarely applied in practice, probably because of severe numerical instabilities. Recently, inspired by the thermodynamic foundations of kinetic theory analyzed by He and Doolen [3], Huang *et al.* [20] developed an LB model with self-tuning equation of state (EOS) for multiphase flows. In this model, a self-tuning EOS is achieved by directly devising the collision term at the discrete level, and a pairwise interaction force is introduced to mimic the long-range molecular interactions that are responsible for the nonmonotonic EOS and nonzero surface tension.

The pseudopotential LB model and the recent LB model with self-tuning EOS can be classified as a class of multiphase LB models based on pairwise interactions. For the pseudopotential LB model, the thermodynamic consistency cannot be achieved in the strict sense [3], and as a compromise solution, various specialized forcing schemes have been proposed to alleviate the inconsistency about coexistence densities (i.e., to approximate the coexistence densities close to the thermodynamic results). Kupershtokh *et al.* [21,22] proposed the exact-difference-method (EDM) forcing scheme, which can help to achieve a relatively low reduced temperature in practice. Huang *et al.* [23] compared five existing forcing schemes and observed that different forcing schemes have quite different performance. In 2012, Li *et al.* [24] found that such difference is mainly caused by the additional term introduced by the forcing scheme in the recovered macroscopic equation, which yields a different coefficient ϵ in the mechanical stability

*rongzong.huang@csu.edu.cn

†whysrj@sjtu.edu.cn

‡nikolaus.adams@tum.de

condition that can be expressed as [25]

$$\int_{\rho_g}^{\rho_l}(P_0 - p_{\rm EOS})\frac{\psi'}{\psi^{1+\epsilon}}d\rho = 0. \tag{1}$$

Here, ρ_g and ρ_l are the coexistence gas and liquid densities, respectively, $p_{\rm EOS}$ denotes the nonmonotonic EOS for multiphase fluids, $P_0 = p_{\rm EOS}(\rho_g) = p_{\rm EOS}(\rho_l)$ is the pressure in the bulk phases, ψ is the so-called pseudopotential, and $\psi' = d\psi/d\rho$. Based on this finding, Li *et al.* [24] proposed an improved forcing scheme that permits to adjust the coefficient ϵ. Afterward, some other specialized forcing schemes that can adjust ϵ were proposed [26–28]. Realizing that there exists some inconsistency in performing the Chapman-Enskog (CE) analysis for the pseudopotential LB model with a specialized forcing scheme, Huang and Wu [29] proposed a consistent scheme for ε^3-order term that can adjust both the coefficient ϵ and surface tension (ε is the small expansion parameter in the CE analysis). As for the recent LB model with self-tuning EOS, the thermodynamic consistency can be naturally achieved, and thus the standard forcing scheme (defined in Sec. II C) is used to incorporate the pairwise interaction force. To compensate for the discrete lattice effect at the ε^3 order, a consistent scheme for ε^3-order term is also employed in this model [20].

For the multiphase LB models based on pairwise interactions, both the specialized forcing scheme and the consistent scheme for ε^3-order term are usually related to the pairwise interaction force, which cannot be simply viewed as a second-order gradient operator due to its explicit physical significance. Therefore, at first glance, the derivatives in density (or effective density, i.e., pseudopotential) do not seem to be involved in this class of multiphase LB models. In this work, we will analyze the specialized forcing scheme and the consistent scheme for ε^3-order term in a unified framework to reveal that the density gradient is implicitly involved in these models. Hereafter, the density gradient represents the gradient of effective density (i.e., pseudopotential) for the pseudopotential LB model or the gradient of density for the LB model with self-tuning EOS, respectively. Then, an improved scheme is proposed to calculate the density gradient for the recent LB model with self-tuning EOS due to its thermodynamic consistency. The remainder of this paper is organized as follows. In Sec. II, theoretical analyses are performed to reveal the involvement of density gradient in the pairwise-interaction-based LB models. In Sec. III, the recent LB model with self-tuning EOS is focused on and an improved scheme is proposed to calculate the density gradient. Analytical and numerical calculations are carried out in Sec. IV to validate the improved scheme, and a brief conclusion is drawn in Sec. V.

II. MULTIPHASE LB MODELS

The multiple-relaxation-time (MRT) LB equation for the density distribution function (DF) f_i can be expressed as [29,30]

$$f_i(\mathbf{x} + \mathbf{e}_i\delta_t, t + \delta_t) = \bar{f}_i(\mathbf{x}, t), \tag{2a}$$

$$\bar{\mathbf{m}}(\mathbf{x}, t) = \mathbf{m} + \delta_t\mathbf{F}_m - \mathbf{S}\left(\mathbf{m} - \mathbf{m}^{\rm eq} + \frac{\delta_t}{2}\mathbf{F}_m\right) + \mathbf{S}\mathbf{Q}_m, \tag{2b}$$

where Eqs. (2a) and (2b) denote the streaming and collision processes executed in velocity and moment spaces, respectively, $\mathbf{m} = \mathbf{M}(f_i)^{\rm T}$ and $(\bar{f}_i)^{\rm T} = \mathbf{M}^{-1}\bar{\mathbf{m}}$ are the moment of density DF and the post-collision density DF, respectively, and $\mathbf{M}$ is the orthogonal transformation matrix [31]. The right-hand side (RHS) of Eq. (2b) is computed at position $\mathbf{x}$ and time t, in which the equilibrium moment $\mathbf{m}^{\rm eq}$ and the discrete force term $\mathbf{F}_m$ are evaluated with the real fluid velocity $\mathbf{u}$, i.e., $\mathbf{m}^{\rm eq} \equiv \mathbf{m}^{\rm eq}(\rho, \mathbf{u})$ and $\mathbf{F}_m \equiv \mathbf{F}_m(\mathbf{F}, \mathbf{u})$. The last term on the RHS of Eq. (2b) is a consistent scheme for ε^3-order term, where the discrete term $\mathbf{Q}_m$ is of order ε^2 (i.e., $\mathbf{Q}_m = \varepsilon^2\mathbf{Q}_m^{(2)}$). The collision matrix $\mathbf{S}$ is diagonal for the pseudopotential LB model, while it is nondiagonal for the recent LB model with self-tuning EOS. The macroscopic variables, density ρ and real fluid velocity $\mathbf{u}$, are defined as

$$\rho = \sum\nolimits_i f_i, \quad \rho\mathbf{u} = \sum\nolimits_i \mathbf{e}_i f_i + \frac{\delta_t}{2}\mathbf{F}. \tag{3}$$

In this work, the two-dimensional nine-velocity (D2Q9) lattice [32] is considered. Therefore, the discrete force term $\mathbf{F}_m$ can be given as [33]

$$\mathbf{F}_m = \left[0,\ 6\frac{\mathbf{F}\cdot\mathbf{u}}{c^2},\ -6\frac{\mathbf{F}\cdot\mathbf{u}}{c^2},\ \frac{F_x}{c},\ -\frac{F_x}{c},\ \frac{F_y}{c},\ -\frac{F_y}{c},\ 2\frac{F_x u_x - F_y u_y}{c^2},\ \frac{F_x u_y + F_y u_x}{c^2}\right]^{\rm T}, \tag{4}$$

where $c = \delta_x/\delta_t$ is the lattice speed. Since this work focuses on the calculation of density gradient, the other technical details (such as $\mathbf{m}^{\rm eq}$ and $\mathbf{S}$), as well as the elimination of the additional cubic terms of velocity, will not be covered here, and the reader is referred to previous works [20,34–36].

In the class of multiphase LB models based on pairwise interactions, the pairwise interaction force is expressed as [12,20]

$$\mathbf{F}(\mathbf{x}) = G^2\phi(\mathbf{x})\sum\nolimits_i \omega(|\mathbf{e}_i\delta_t|^2)\phi(\mathbf{x} + \mathbf{e}_i\delta_t)\mathbf{e}_i\delta_t, \tag{5}$$

where ϕ denotes the pseudopotential ψ for the pseudopotential LB model [12,22,24,29,34] or the density ρ for the LB model with self-tuning EOS [20], G^2 is used to control the interaction strength, and $\omega(|\mathbf{e}_i\delta_t|^2)$ is the weight to maximize the isotropy degree of $\mathbf{F}$. In this work, the nearest-neighbor interaction is considered, and thus $\omega(\delta_x^2) = 1/3$ and $\omega(2\delta_x^2) = 1/12$, which indicates that $\sum_i \omega(|\mathbf{e}_i\delta_t|^2)\mathbf{e}_i\mathbf{e}_i\delta_t^2 = \delta_x^2\mathbf{I}$ and $\sum_i \omega(|\mathbf{e}_i\delta_t|^2)\mathbf{e}_i\mathbf{e}_i\mathbf{e}_i\mathbf{e}_i\delta_t^4 = \delta_x^4\mathbf{II}/3$ [37]. Here $(\mathbf{II})_{\alpha\beta\gamma\delta} = \delta_{\alpha\beta}\delta_{\gamma\delta} + \delta_{\alpha\gamma}\delta_{\beta\delta} + \delta_{\alpha\delta}\delta_{\beta\gamma}$. Performing Taylor series expansion of $\phi(\mathbf{x} + \mathbf{e}_i\delta_t)$ centered at $\mathbf{x}$, $\mathbf{F}$ given by Eq. (5) can be written as

$$\mathbf{F} = G^2\delta_x^2\phi\nabla\phi + \frac{G^2\delta_x^4}{6}\phi\nabla\nabla\cdot\nabla\phi + O(\nabla^5). \tag{6}$$

Based on Eq. (6), a simple scheme can be obtained to calculate $\nabla\phi$ as follows:

$$\nabla\phi = \frac{\mathbf{F}}{G^2\delta_x^2\phi} + O(\nabla^3), \tag{7}$$

which is actually the second-order isotropic central scheme (ICS) simplified with the pairwise interaction force.

A. Specialized forcing schemes

In the LB method, a forcing scheme is used to incorporate the force term and thus consists of all the relevant terms in both the LB equation and the defining equation of macroscopic variables, e.g., $\delta_t(\mathbf{I}-\mathbf{S}/2)\mathbf{F}_m$ in Eq. (2b) and $\delta_t\mathbf{F}/2$ in Eq. (3). To approximate the coexistence densities close to the thermodynamic results, as well as to achieve relatively low reduced temperature, various specialized forcing schemes have been proposed for the pseudopotential LB model. In the following, two popular schemes, proposed by Kupershtokh *et al.* [21,22] and Li *et al.* [24], respectively, will be analyzed.

1. *Kupershtokh* et al.*'s forcing scheme*

The forcing scheme proposed by Kupershtokh *et al.* [21,22] (i.e., the so-called EDM forcing scheme) is widely adopted because of its compact form and good stability with respect to the reduced temperature. It is originally derived for the single-relaxation-time (SRT) LB equation, which is given as [22]

$$f_i(\mathbf{x}+\mathbf{e}_i\delta_t, t+\delta_t) = f_i - \frac{1}{\tau}\left[f_i - f_i^{\mathrm{eq}}(\rho,\mathbf{v})\right] + \left[f_i^{\mathrm{eq}}(\rho,\mathbf{v}+\delta\mathbf{v}) - f_i^{\mathrm{eq}}(\rho,\mathbf{v})\right], \quad (8)$$

where $\mathbf{v}=\sum_i \mathbf{e}_i f_i/\rho$, $\delta\mathbf{v}=\delta_t\mathbf{F}/\rho$, τ is the dimensionless relaxation time, $f_i^{\mathrm{eq}}(\rho,\mathbf{v})$ and $f_i^{\mathrm{eq}}(\rho,\mathbf{v}+\delta\mathbf{v})$ are the equilibrium density DFs evaluated with $\mathbf{v}$ and $\mathbf{v}+\delta\mathbf{v}$, respectively, and the RHS is computed at position $\mathbf{x}$ and time t. The macroscopic density ρ and velocity $\mathbf{u}$ are also defined by Eq. (3), which suggests that $\mathbf{u}=\mathbf{v}+\delta\mathbf{v}/2$. The above SRT LB equation can be easily extended to MRT LB equation. The corresponding MRT collision process in moment space is expressed as

$$\bar{\mathbf{m}}(\mathbf{x},t) = \mathbf{m} - \mathbf{S}[\mathbf{m}-\mathbf{m}^{\mathrm{eq}}(\rho,\mathbf{v})] + [\mathbf{m}^{\mathrm{eq}}(\rho,\mathbf{v}+\delta\mathbf{v}) - \mathbf{m}^{\mathrm{eq}}(\rho,\mathbf{v})]. \quad (9)$$

In the CE analysis, $\mathbf{u}$ is of order ε^0 and $\mathbf{F}$ is of order ε^1. Therefore, to avoid the inconsistency in performing the CE analysis for EDM forcing scheme, $\mathbf{v}$ and $\delta\mathbf{v}$ should be substituted by $\mathbf{u}-\delta_t\mathbf{F}/(2\rho)$ and $\delta_t\mathbf{F}/\rho$, respectively, and $\mathbf{m}^{\mathrm{eq}}(\rho,\mathbf{v})$ and $\mathbf{m}^{\mathrm{eq}}(\rho,\mathbf{v}+\delta\mathbf{v})$ should also be decomposed [38]. On the basis of this principle, Eq. (9) is reformulated as [29]

$$\bar{\mathbf{m}}(\mathbf{x},t) = \mathbf{m} + \delta_t\mathbf{F}_m - \mathbf{S}\left[\mathbf{m}-\mathbf{m}^{\mathrm{eq}}(\rho,\mathbf{u}) + \frac{\delta_t}{2}\mathbf{F}_m\right] + \mathbf{S}\mathbf{Q}_{m,\mathrm{EDM}}, \quad (10)$$

where $\mathbf{m}^{\mathrm{eq}}(\rho,\mathbf{u})$ is evaluated with the real fluid velocity $\mathbf{u}$, $\mathbf{F}_m$ is the same as Eq. (4), and the discrete term $\mathbf{Q}_{m,\mathrm{EDM}}$ is given as

$$\mathbf{Q}_{m,\mathrm{EDM}} = \left[0,\ \frac{3}{4}\frac{\delta_t^2|\mathbf{F}|^2}{\rho c^2},\ -\frac{3}{4}\frac{\delta_t^2|\mathbf{F}|^2}{\rho c^2},\ 0,\ 0,\ 0,\ 0,\ \frac{1}{4}\frac{\delta_t^2(F_x^2-F_y^2)}{\rho c^2},\ \frac{1}{4}\frac{\delta_t^2F_xF_y}{\rho c^2}\right]^{\mathrm{T}}. \quad (11)$$

Although the form of Eq. (10) seems to be more complicated than the form of Eq. (9), Eq. (10) is a better starting point for performing the consistent CE analysis, because $\mathbf{m}^{\mathrm{eq}}(\rho,\mathbf{u})$, $\mathbf{F}_m$, and $\mathbf{Q}_{m,\mathrm{EDM}}$ in Eq. (10) are of order ε^0, ε^1, and ε^2, respectively.

2. *Li* et al.*'s forcing scheme*

The forcing scheme proposed by Li *et al.* [24] is widely adopted in practice because of its ability to adjust the coefficient ϵ in mechanical stability condition. The SRT LB equation with Li *et al.*'s forcing scheme is given as [24]

$$f_i(\mathbf{x}+\mathbf{e}_i\delta_t, t+\delta_t) = f_i - \frac{1}{\tau}\left[f_i - f_i^{\mathrm{eq}}(\rho,\mathbf{u})\right] + \delta_t\omega_i\left(1-\frac{1}{2\tau}\right)\left(\frac{\mathbf{e}_i-\mathbf{u}'}{c_s^2} + \frac{\mathbf{e}_i\cdot\mathbf{u}'}{c_s^4}\mathbf{e}_i\right)\cdot\mathbf{F}, \quad (12)$$

where $c_s=c/\sqrt{3}$, $\mathbf{u}'=\mathbf{u}+\sigma\mathbf{F}/[(\tau-0.5)\psi^2]$, and σ is used to adjust the coefficient ϵ. Similarly, the RHS of Eq. (12) is computed at $(\mathbf{x},t)$, and the macroscopic variables, density ρ and velocity $\mathbf{u}$, are defined by Eq. (3). An MRT version of Li *et al.*'s forcing scheme can be obtained based on Eq. (12). The corresponding MRT collision process in moment space is expressed as

$$\bar{\mathbf{m}}(\mathbf{x},t) = \mathbf{m} - \mathbf{S}[\mathbf{m}-\mathbf{m}^{\mathrm{eq}}(\rho,\mathbf{u})] + \delta_t\left(\mathbf{I}-\frac{\mathbf{S}}{2}\right)\mathbf{F}_{m,\mathrm{Li}}, \quad (13)$$

where $\mathbf{F}_{m,\mathrm{Li}}$ is given as

$$\mathbf{F}_{m,\mathrm{Li}} = \left[0,\ 6\frac{\mathbf{F}\cdot\mathbf{u}}{c^2} + 6\sigma\frac{|\mathbf{F}|^2}{(s_e^{-1}-0.5)\psi^2c^2},\ -6\frac{\mathbf{F}\cdot\mathbf{u}}{c^2} - 6\sigma\frac{|\mathbf{F}|^2}{(s_\varepsilon^{-1}-0.5)\psi^2c^2},\ \frac{F_x}{c},\ -\frac{F_x}{c},\ \frac{F_y}{c},\ -\frac{F_y}{c},\ 2\frac{F_xu_x-F_yu_y}{c^2} + 2\sigma\frac{F_x^2-F_y^2}{(s_p^{-1}-0.5)\psi^2c^2},\ \frac{F_xu_y+F_yu_x}{c^2} + 2\sigma\frac{F_xF_y}{(s_p^{-1}-0.5)\psi^2c^2}\right]^{\mathrm{T}}. \quad (14)$$

Note that $\tau-0.5$ in $\mathbf{u}'$ is replaced by $s_e^{-1}-0.5$, $s_\varepsilon^{-1}-0.5$, or $s_p^{-1}-0.5$ when deriving the above $\mathbf{F}_{m,\mathrm{Li}}$. Here, s_e, s_ε, and s_p are the relaxation parameters in $\mathbf{S}$ [29]. Since $\mathbf{u}$ is of order ε^0 and $\mathbf{F}$ is of order ε^1, $\mathbf{F}_{m,\mathrm{Li}}$ consists of two parts that are of order ε^1 and ε^2, respectively. To facilitate the consistent CE analysis for Li *et al.*'s forcing scheme, Eq. (13) can be reformulated as

$$\bar{\mathbf{m}}(\mathbf{x},t) = \mathbf{m}+\delta_t\mathbf{F}_m-\mathbf{S}\left[\mathbf{m}-\mathbf{m}^{\mathrm{eq}}(\rho,\mathbf{u}) + \frac{\delta_t}{2}\mathbf{F}_m\right] + \mathbf{S}\mathbf{Q}_{m,\mathrm{Li}}, \quad (15)$$

where $\mathbf{F}_m$ is the same as Eq. (4) and the discrete term $\mathbf{Q}_{m,\mathrm{Li}}$ is given as

$$\mathbf{Q}_{m,\mathrm{Li}} = \left[0,\ 6\sigma\frac{\delta_t|\mathbf{F}|^2}{\psi^2c^2},\ -6\sigma\frac{\delta_t|\mathbf{F}|^2}{\psi^2c^2},\ 0,\ 0,\ 0,\ 0,\ 2\sigma\frac{\delta_t(F_x^2-F_y^2)}{\psi^2c^2},\ 2\sigma\frac{\delta_tF_xF_y}{\psi^2c^2}\right]^{\mathrm{T}}. \quad (16)$$

Obviously, $\mathbf{m}^{\mathrm{eq}}(\rho,\mathbf{u})$, $\mathbf{F}_m$, and $\mathbf{Q}_{m,\mathrm{Li}}$ in Eq. (15) are of order ε^0, ε^1, and ε^2, respectively.

B. Consistent schemes for ε^3-order term

To avoid the inconsistency in performing the CE analysis for the pseudopotential LB model with a specialized forcing scheme, Huang and Wu [29] proposed a consistent scheme for ε^3-order term for the pseudopotential LB model. A similar scheme is also employed in the recent LB model with self-tuning EOS [20]. For these pairwise-interaction-based LB models with a consistent scheme for ε^3-order term, the MRT LB equation is generally written as Eq. (2), and the macroscopic density and velocity are defined by Eq. (3).

1. Pseudopotential LB model

For the pseudopotential LB model, to adjust the coefficient ϵ in mechanical stability condition and the surface tension, Huang and Wu proposed the following discrete term [29]

$$\mathbf{Q}_m = \left[0,\ -3(k_1+2k_2)\frac{|\mathbf{F}|^2}{G^2\psi^2c^2},\ 3(k_1+2k_2)\frac{|\mathbf{F}|^2}{G^2\psi^2c^2},\right.$$
$$\left.0,\ 0,\ 0,\ 0,\ -k_1\frac{F_x^2-F_y^2}{G^2\psi^2c^2},\ -k_1\frac{F_xF_y}{G^2\psi^2c^2}\right]^{\mathrm{T}}, \quad (17)$$

where k_1 and k_2 are the adjustable parameters, and G is the same as that in the pairwise interaction force given by Eq. (5), which is different from the G in the original work by Huang and Wu [29].

2. LB model with self-tuning EOS

Recently, a thermodynamically consistent LB model with self-tuning EOS is developed by Huang *et al.* [20]. To compensate for the discrete lattice effect at the ε^3 order, a consistent scheme for ε^3-order term is employed in this model. The corresponding discrete term is given as [20]

$$\mathbf{Q}_m = \left[0,\ \frac{1}{2}\frac{|\mathbf{F}|^2}{G^2\rho^2c^2},\ -\frac{1}{2}\frac{|\mathbf{F}|^2}{G^2\rho^2c^2},\ 0,\ 0,\ 0,\ 0,\right.$$
$$\left.\frac{1}{12}\frac{F_x^2-F_y^2}{G^2\rho^2c^2},\ \frac{1}{12}\frac{F_xF_y}{G^2\rho^2c^2}\right]^{\mathrm{T}}. \quad (18)$$

Note that the LB model with self-tuning EOS is naturally consistent with thermodynamic theory, and the surface tension can be adjusted by the scaling factors in both the adopted EOS and interaction strength. Therefore, $\mathbf{Q}_m$ for this model [i.e., Eq. (18)] does not contain any adjustable parameters, which is different from $\mathbf{Q}_m$ for the pseudopotential LB model [i.e., Eq. (17)].

C. Discussions

From the above analyses, we can see that Eqs. (2), (3), and (4) can be viewed as a unified framework for the pairwise-interaction-based LB models with a specialized forcing scheme or with a consistent scheme for ε^3-order term. The forcing scheme, constituted by $\delta_t(\mathbf{I}-\mathbf{S}/2)\mathbf{F}_m$ in Eq. (2b), $\delta_t\mathbf{F}/2$ in Eq. (3), and $\mathbf{F}_m$ given by Eq. (4), can be regarded as a standard forcing scheme, which is first proposed by Guo *et al.* [33] and can be derived from the kinetic theory in an *a priori* manner. The discrete term $\mathbf{Q}_m$ can be generally written as

$$\mathbf{Q}_m = [0,\ Q_{m,1},\ Q_{m,2},\ 0,\ 0,\ 0,\ 0,\ Q_{m,7},\ Q_{m,8}]^{\mathrm{T}}. \quad (19)$$

Through the third-order CE analysis, the ε^3-order term $\mathbf{R}_{\mathrm{add}}$ introduced by $\mathbf{SQ}_m$ in the recovered macroscopic momentum conservation equation can be derived [29]

$$\mathbf{R}_{\mathrm{add}} = -c^2\begin{bmatrix}\partial_x\left(\frac{1}{6}Q_{m,1}+\frac{1}{2}Q_{m,7}\right)+\partial_yQ_{m,8}\\ \partial_xQ_{m,8}+\partial_y\left(\frac{1}{6}Q_{m,1}-\frac{1}{2}Q_{m,7}\right)\end{bmatrix}. \quad (20)$$

Based on the specific $\mathbf{Q}_m$ given by Eqs. (11), (16), (17), and (18), $\mathbf{R}_{\mathrm{add}}$ can be generally written as

$$\mathbf{R}_{\mathrm{add}} = \nabla\cdot\left[A_1\frac{\mathbf{FF}}{G^2\phi^2}+A_2\frac{(\mathbf{F}\cdot\mathbf{F})\mathbf{I}}{G^2\phi^2}\right], \quad (21)$$

where $A_1=-\delta_t^2G^2\psi^2/(4\rho)$ and $A_2=0$ for Kupershtokh *et al.*'s forcing scheme, $A_1=-2\sigma\delta_tG^2$ and $A_2=0$ for Li *et al.*'s forcing scheme, $A_1=k_1$ and $A_2=k_2$ for the consistent scheme for ε^3-order term in the pseudopotential LB model, and $A_1=-1/12$ and $A_2=-1/24$ for the consistent scheme for ε^3-order term in the LB model with self-tuning EOS. Here, it is worth pointing out that A_1 for Kupershtokh *et al.*'s forcing scheme varies with space and time due to its factor ψ^2/ρ, while A_1 and A_2 for the other schemes are constants. Since $\nabla=\varepsilon^1\nabla_1$ and $\mathbf{F}=\varepsilon^1\mathbf{F}^{(1)}$ in the CE analysis, $\mathbf{R}_{\mathrm{add}}$ given by Eq. (21) is consistently of order ε^3. In the multiphase LB models based on pairwise interactions, the ε^3-order term $\mathbf{R}_{\mathrm{add}}$ should be considered in deriving the correct pressure tensor [20,24,29], and Eq. (7) [i.e., $\nabla\phi=\mathbf{F}/(G^2\delta_x^2\phi)$] can be used for further calculation. Considering Eq. (7), $\mathbf{R}_{\mathrm{add}}$ given by Eq. (21) can be simplified as

$$\mathbf{R}_{\mathrm{add}} = \nabla\cdot\left[A_1G^2\delta_x^4\nabla\phi\nabla\phi+A_2G^2\delta_x^4(\nabla\phi\cdot\nabla\phi)\mathbf{I}\right], \quad (22)$$

and the corresponding term $\mathbf{P}_{\mathrm{add}}$ introduced by $\mathbf{R}_{\mathrm{add}}$ in the derived pressure tensor ($\nabla\cdot\mathbf{P}_{\mathrm{add}}\equiv-\mathbf{R}_{\mathrm{add}}$) is

$$\mathbf{P}_{\mathrm{add}} = -A_1G^2\delta_x^4\nabla\phi\nabla\phi-A_2G^2\delta_x^4(\nabla\phi\cdot\nabla\phi)\mathbf{I}. \quad (23)$$

For the multiphase LB models based on pairwise interactions, the pairwise interaction force, given by Eq. (5) and incorporated by the standard forcing scheme, cannot be simply viewed as a finite-difference gradient operator due to its explicit physical significance. However, the ε^3-order term $\mathbf{R}_{\mathrm{add}}$, introduced by the specialized forcing scheme or the consistent scheme for ε^3-order term, should be viewed as a numerical trick without explicit physical significance to alleviate the thermodynamic inconsistency about the coexistence densities or to compensate for the discrete lattice effect at the ε^3 order. From this viewpoint, $\nabla\phi$ is actually involved in the pairwise-interaction-based LB models via the ε^3-order term $\mathbf{R}_{\mathrm{add}}$ [see Eq. (22)], and this $\nabla\phi$ is calculated by the second-order ICS simplified with the pairwise interaction force [i.e., Eq. (7)] in previous works. Theoretically speaking, it is unnecessary to calculate $\nabla\phi$ for $\mathbf{R}_{\mathrm{add}}$ via Eq. (7). In addition, it is more reasonable to express $\mathbf{Q}_m$ in terms of $\nabla\phi$ rather than in terms of $\mathbf{F}$. Therefore, $\mathbf{Q}_m$ given by Eqs. (11), (16), (17), and (18) can be generally expressed as

$$\mathbf{Q}_m = -G^2\delta_x^2\delta_t^2\left[0,\ 3(A_1+2A_2)|\nabla\phi|^2,\ -3(A_1+2A_2)|\nabla\phi|^2,\right.$$
$$\left.0,\ 0,\ 0,\ 0,\ A_1[(\partial_x\phi)^2-(\partial_y\phi)^2],\ A_1\partial_x\phi\partial_y\phi\right]^{\mathrm{T}}, \quad (24)$$

where A_1 and A_2 are the same as those in Eq. (21).

Due to its explicit physical significance, the pairwise interaction force **F**, which is incorporated by the standard forcing scheme, is relatively accurate in simulating multiphase flows by the pairwise-interaction-based LB models. However, as a numerical trick, the ε^3-order term $\mathbf{R}_{\text{add}}$, which is generally introduced by the term $\mathbf{S}\mathbf{Q}_m$ in Eq. (2b), could be a major source of numerical error. To verify this point, a one-dimensional flat interface is simulated by the pseudopotential LB model with consistent scheme for ε^3-order term [i.e., Eq. (17)]. Three sets of k_1 and k_2 are considered, i.e., (i) $k_1 = 0$ and $k_2 = 0$, (ii) $k_1 = -1/8$ and $k_2 = 0$, and (iii) $k_1 = -1/4$ and $k_2 = 0$, which correspond to the coefficient ϵ in mechanical stability condition being 0, 1, and 2, respectively. The Carnahan-Starling EOS [see Eq. (29)], with $a = 1$, $b = 4$, $R_g = 1$, and $K_{\text{EOS}} = 1/4$, is adopted in the simulations. The interaction strength, lattice spacing, and time step are chosen as $G = 1$, $\delta_x = 1$, and $\delta_t = 1$, respectively.

The numerical results are shown in Fig. 1. For the case with $k_1 = 0$ and $k_2 = 0$ (i.e., $\mathbf{Q}_m = \mathbf{0}$), the coexistence curve obtained by simulation is in excellent agreement with the analytical one given by mechanical stability condition, as seen from Fig. 1(a). To be quantitative, at the reduced temperature $T_r = 0.76156$, the analytical gas and liquid densities ($\rho_{g,\text{analytical}}$ and $\rho_{l,\text{analytical}}$) are $1.32696253 \times 10^{-6}$ and $3.23474688 \times 10^{-1}$, respectively, while the numerical gas and liquid densities ($\rho_{g,\text{numerical}}$ and $\rho_{l,\text{numerical}}$) are $1.32697638 \times 10^{-6}$ and $3.23474688 \times 10^{-1}$, respectively. For the other two cases with $k_1 \neq 0$ and $k_2 = 0$ (i.e., $\mathbf{Q}_m \neq \mathbf{0}$), the coexistence curve by simulation agrees with the analytical one by mechanical stability condition when T_r is relatively large. However, the deviation in gas branch becomes quite obvious when T_r is relatively low. Quantitatively, for the case with $k_1 = -1/8$ and $k_2 = 0$, the analytical and numerical gas densities are $1.21325731 \times 10^{-6}$ and $5.76969968 \times 10^{-6}$, respectively, at $T_r = 0.650$; as for the case with $k_1 = -1/4$ and $k_2 = 0$, the analytical and numerical gas densities are $7.87354321 \times 10^{-5}$ and $1.63470555 \times 10^{-4}$, respectively, at $T_r = 0.400$. Considering the deviation in gas branch is much larger than the deviation in liquid branch, the relative error of gas density ($E_{\rho,\text{gas}} = |\rho_{g,\text{numerical}} - \rho_{g,\text{analytical}}|/\rho_{g,\text{analytical}}$) is computed here, and the variation of $E_{\rho,\text{gas}}$ with the analytical liquid-to-gas density ratio ($\rho_{l,\text{analytical}}/\rho_{g,\text{analytical}}$) is given in Fig. 1(b). As one can see, at the same density ratio $\rho_{l,\text{analytical}}/\rho_{g,\text{analytical}}$, $E_{\rho,\text{gas}}$ with $\mathbf{Q}_m = \mathbf{0}$ is about five orders of magnitude smaller than $E_{\rho,\text{gas}}$ with $\mathbf{Q}_m \neq \mathbf{0}$. Here, it is worth emphasizing that the gas density obtained with $\mathbf{Q}_m = \mathbf{0}$ greatly deviates from the thermodynamic result given by Maxwell construction, even though the corresponding $E_{\rho,\text{gas}}$ is very small. In the practical applications of the pseudopotential LB model, a suitable nonzero $\mathbf{Q}_m$ is necessary to approximate the gas density close to the thermodynamic result [22,24,29].

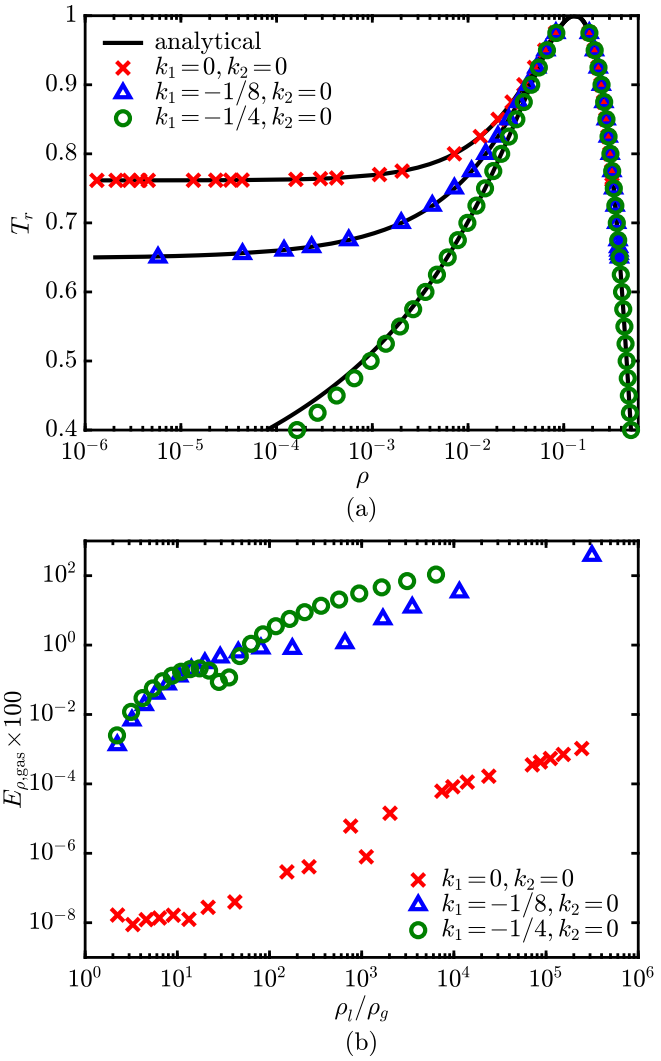

FIG. 1. Numerical results for the simulations of one-dimensional flat interface by the pseudopotential LB model with consistent scheme for ε^3-order term. (a) The coexistence curves obtained by simulation and the analytical ones given by mechanical stability condition. (b) The relative error of gas density $E_{\rho,\text{gas}} = |\rho_{g,\text{numerical}} - \rho_{g,\text{analytical}}|/\rho_{g,\text{analytical}}$ versus the analytical density ratio $\rho_{l,\text{analytical}}/\rho_{g,\text{analytical}}$.

III. DENSITY GRADIENT CALCULATION

From the above analyses, it can be seen that $\nabla\phi$ is generally involved in the pairwise-interaction-based LB models and this $\nabla\phi$ is simply calculated by Eq. (7) in previous works. In the following, we will focus on the recent LB model with self-tuning EOS due to its thermodynamic consistency and then propose an improved scheme to calculate the density gradient ($\phi = \rho$). In this model, the discrete term $\mathbf{Q}_m$ [see Eqs. (18) and (24)] can be expressed in terms of $\nabla\rho$ as follows:

$$\mathbf{Q}_m = G^2\delta_x^2\delta_t^2\Big[0,\ \frac{1}{2}|\nabla\rho|^2,\ -\frac{1}{2}|\nabla\rho|^2,\ 0,\ 0,\ 0,\ 0,\ \frac{1}{12}[(\partial_x\rho)^2 - (\partial_y\rho)^2],\ \frac{1}{12}\partial_x\rho\partial_y\rho\Big]^{\mathrm{T}}, \tag{25}$$

and the derived pressure tensor **P** satisfies [20]

$$\nabla\cdot\mathbf{P} = \nabla p_{\text{EOS}} - \kappa\rho\nabla\nabla\cdot\nabla\rho, \tag{26}$$

where $\kappa = G^2\delta_x^2/4$ and p_{EOS} is the recovered EOS for multiphase fluids.

For the single-phase flows under the low Mach number condition, it has been shown that the pressure can be

decomposed into the dynamic and thermodynamic parts, where the dynamic part acts to balance the inertia and external force and the thermodynamic part can be assumed to be spatially uniform [39]. Inspired by this idea, and considering that the LB model is limited to the low Mach number flows, we assume that the pressure tensor recovered by the multiphase LB model is spatially uniform (i.e., $\nabla \cdot \mathbf{P} = \mathbf{0}$) to calculate the density gradient. Therefore, from Eq. (26), we have

$$\nabla p_{\mathrm{EOS}} = \kappa \rho \nabla \nabla \cdot \nabla \rho, \tag{27}$$

where ∇p_{EOS} can be further written as $\frac{dp_{\mathrm{EOS}}}{d\rho}\nabla\rho$. Substituting Eq. (27) into the Taylor series expansion of the pairwise interaction force [i.e., Eq. (6)], an improved scheme for $\nabla\rho$ can be obtained

$$\nabla \rho = \frac{\mathbf{F}}{G^2 \delta_x^2 \rho + \frac{2}{3}\frac{dp_{\mathrm{EOS}}}{d\rho}}. \tag{28}$$

In practical applications, the EOS p_{EOS} is directly specified, and $\frac{dp_{\mathrm{EOS}}}{d\rho}$ can be easily obtained. Compared with the previous second-order ICS [i.e., Eq. (7)], the present improved scheme does not introduce additional complexity in the multiphase LB model. Here, it is worth pointing out that the low Mach number approximation $\nabla \cdot \mathbf{P} = \mathbf{0}$ is only used to calculate $\nabla\rho$ in the discrete term $\mathbf{Q}_m$ [i.e., Eq. (25)] for the ε^3-order term $\mathbf{R}_{\mathrm{add}}$.

IV. VALIDATIONS AND DISCUSSIONS

In this section, analytical and numerical calculations are carried out to validate the improved scheme for density gradient for the LB model with self-tuning EOS. The Carnahan-Starling EOS is chosen as an example [40],

$$p_{\mathrm{EOS}} = K_{\mathrm{EOS}}\left[\rho R_g T \frac{1+\vartheta+\vartheta^2-\vartheta^3}{(1-\vartheta)^3} - a\rho^2\right], \tag{29}$$

where R_g is the gas constant, T is the temperature, and $\vartheta = b\rho/4$. Here, the coefficients a and b are related to the critical point as $a = 0.4963880577294099 R_g^2 T_c^2/p_c$ and $b = 0.1872945669467330 R_g T_c/p_c$, with T_c and p_c denoting the critical temperature and pressure, respectively. In the following, $a = 1$, $b = 4$, and $R_g = 1$ are chosen, and the reduced temperature is given as $T_r = T/T_c$. For the LB model with self-tuning EOS, the interaction strength is set to [20]

$$G = K_{\mathrm{INT}}\sqrt{2K_{\mathrm{EOS}}a/\delta_x^2}, \tag{30}$$

and the lattice sound speed is chosen as

$$c_s = K_{\mathrm{INT}}\sqrt{\partial_\rho(p_{\mathrm{EOS}} + K_{\mathrm{EOS}}a\rho^2)}\Big|_{\rho=\rho_l}. \tag{31}$$

In Eqs. (29), (30), and (31), the scaling factors K_{EOS} and K_{INT} are used to adjust the surface tension σ and interface thickness W, which satisfy $\sigma \propto K_{\mathrm{EOS}}K_{\mathrm{INT}}$ and $W \propto K_{\mathrm{INT}}$, respectively. In this work, the interface thickness W is defined from $\rho = 0.95\rho_g + 0.05\rho_l$ to $\rho = 0.05\rho_g + 0.95\rho_l$. More technical details of this LB model (such as $\mathbf{m}^{\mathrm{eq}}$ and $\mathbf{S}$) can be found in Ref. [20].

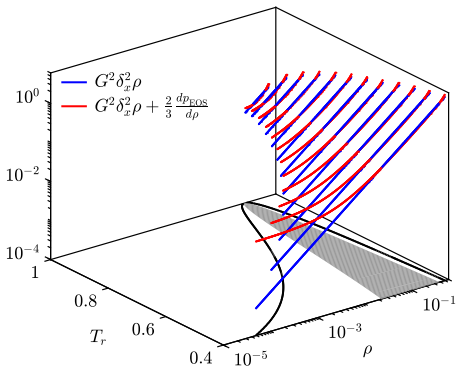

FIG. 2. Comparisons between the denominator $G^2\delta_x^2\rho + \frac{2}{3}\frac{dp_{\mathrm{EOS}}}{d\rho}$ of Eq. (28) and the denominator $G^2\delta_x^2\rho$ of Eq. (7). The scaling factor K_{INT} is determined by prescribing $W = 5\delta_x$, and the scaling factor K_{EOS} is fixed at 1. In the ρ-T_r plane, the coexistence curve by Maxwell construction is shown by the solid line and the region with $\frac{dp_{\mathrm{EOS}}}{d\rho} < 0$ is depicted by the gray area.

Before proceeding further, some discussion on the denominator $G^2\delta_x^2\rho + \frac{2}{3}\frac{dp_{\mathrm{EOS}}}{d\rho}$ of the improved scheme for density gradient [i.e., Eq. (28)] is necessary. As it is known, the EOS for multiphase fluids is nonmonotonic, implying that $\frac{dp_{\mathrm{EOS}}}{d\rho}$ could be negative. To show the magnitude and variation of $\frac{dp_{\mathrm{EOS}}}{d\rho}$, the denominator $G^2\delta_x^2\rho + \frac{2}{3}\frac{dp_{\mathrm{EOS}}}{d\rho}$ of Eq. (28) is calculated and compared with the denominator $G^2\delta_x^2\rho$ of Eq. (7). The scaling factor K_{INT} is determined by prescribing $W = 5\delta_x$, which is quite small in real simulations. The scaling factor K_{EOS} has no effect on the relative magnitude and variation of $\frac{dp_{\mathrm{EOS}}}{d\rho}$, and thus K_{EOS} is simply fixed at 1. The results with T_r varying from 0.95 to 0.40 are given in Fig. 2, where the coexistence curve by Maxwell construction is shown by the solid line and the region with $\frac{dp_{\mathrm{EOS}}}{d\rho} < 0$ is depicted by the gray area in the ρ-T_r plane. It can be seen from Fig. 2 that $\frac{dp_{\mathrm{EOS}}}{d\rho}$ is negative in the middle-density range (also see Fig. 6), and $G^2\delta_x^2\rho + \frac{2}{3}\frac{dp_{\mathrm{EOS}}}{d\rho}$, just like $G^2\delta_x^2\rho$, is invariably positive. In the region with $\frac{dp_{\mathrm{EOS}}}{d\rho} < 0$, $G^2\delta_x^2\rho + \frac{2}{3}\frac{dp_{\mathrm{EOS}}}{d\rho}$ is slightly smaller than $G^2\delta_x^2\rho$, while in the region with $\frac{dp_{\mathrm{EOS}}}{d\rho} > 0$ and near the gas branch, $G^2\delta_x^2\rho + \frac{2}{3}\frac{dp_{\mathrm{EOS}}}{d\rho}$ could be significantly larger than $G^2\delta_x^2\rho$ when T_r is relatively low. As the interface thickness increases, the gap between $G^2\delta_x^2\rho + \frac{2}{3}\frac{dp_{\mathrm{EOS}}}{d\rho}$ and $G^2\delta_x^2\rho$ tends to become smaller, which is expected since the accuracy of Eq. (7) can be systematically improved by grid refinement. From the above discussion, it can be found that as compared with the denominator $G^2\delta_x^2\rho$ of Eq. (7), the denominator $G^2\delta_x^2\rho + \frac{2}{3}\frac{dp_{\mathrm{EOS}}}{d\rho}$ of Eq. (28) will not become rather small in spite of the negative $\frac{dp_{\mathrm{EOS}}}{d\rho}$.

A. One-dimensional flat interface

First, a one-dimensional flat interface put along the y coordinate is considered. From Eq. (26), the following pressure tensor can be derived:

$$\mathbf{P} = \left(p_{\mathrm{EOS}} - \kappa\rho\nabla\cdot\nabla\rho - \frac{\kappa}{2}\nabla\rho\cdot\nabla\rho\right)\mathbf{I} + \kappa\nabla\rho\nabla\rho, \tag{32}$$

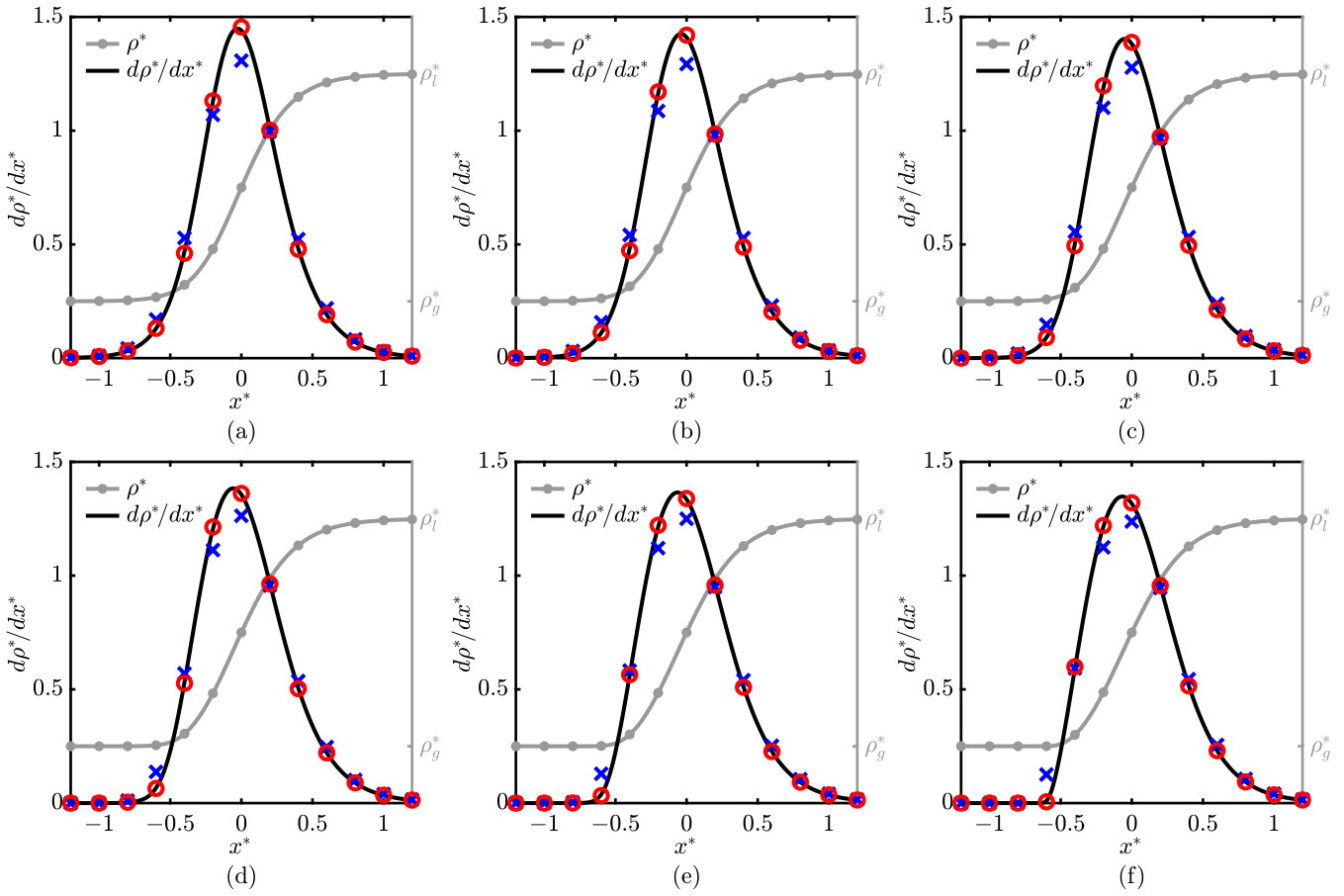

FIG. 3. The profiles of normalized density ρ^* and density gradient $d\rho^*/dx^*$ across phase interface. The solid lines are the analytical profiles, the dot denotes the density ρ^* at the grid point set to its analytical value, and the cross and circle denote the density gradient $d\rho^*/dx^*$ at the grid point calculated by Eqs. (7) and (28), respectively. The reduced temperature is chosen as (a) $T_r = 0.9$, (b) $T_r = 0.8$, (c) $T_r = 0.7$, (d) $T_r = 0.6$, (e) $T_r = 0.5$, and (f) $T_r = 0.4$, respectively.

and thus the normal pressure is given as

$$P_n = p_{\mathrm{EOS}} - \kappa\rho\frac{d^2\rho}{dx^2} + \frac{\kappa}{2}\left(\frac{d\rho}{dx}\right)^2. \tag{33}$$

In the equilibrium state, the normal pressure should be equal to the pressure in the bulk gas and liquid phases. Therefore, from Eq. (33) and following the procedure in Ref. [12], the following integral equation can be obtained [41]:

$$\int_{\rho_g}^{\rho_l}(P_0 - p_{\mathrm{EOS}})\frac{1}{\rho^2}d\rho = 0, \tag{34}$$

where $P_0 = p_{\mathrm{EOS}}(\rho_g) = p_{\mathrm{EOS}}(\rho_l)$ is the pressure in the bulk phases. Equation (34) is known as the Maxwell construction in thermodynamic theory, from which the coexistence densities can be thermodynamically determined.

To validate the improved scheme for density gradient, the analytical profiles of density and density gradient across phase interface are computed from Eqs. (33) and (34) using numerical integration. Then, the spatial discretization is carried out with the interfacial region being divided into five grid points (i.e., $W/\delta_x = 5$), and the density at the grid point is set to its analytical value. Based on the density at the grid point, the density gradient at the grid point is calculated by Eqs. (7) and (28), respectively. For the sake of discussion, the density and coordinate are normalized as $\rho^* = (\rho - \rho_g)/(\rho_l - \rho_g)$ and $x^* = x/W$, respectively, and $K_{\mathrm{EOS}} = K_{\mathrm{INT}} = 1$ are used in the computations because the profiles of ρ^* and $d\rho^*/dx^*$ are independent of K_{EOS} and K_{INT}. The results with T_r varying from 0.9 to 0.4 are given in Fig. 3. It can be seen that $d\rho^*/dx^*$ calculated by Eq. (28) agrees very well with its analytical value, while $d\rho^*/dx^*$ calculated by Eq. (7) obviously deviates from its analytical value in the interfacial region, especially around $x^* = -0.6$ and $x^* = 0$. Thus, the present improved scheme [i.e., Eq. (28)] is more accurate than the previous second-order ICS [i.e., Eq. (7)]. From Fig. 3, the asymmetry of the $d\rho^*/dx^*$ profile with respect to $x^* = 0$ can be clearly seen, especially when T_r is relatively low. Such a feature indicates that the equilibrium density profile across phase interface considerably deviates from a hyperbolic tangent function for the Carnahan-Starling EOS.

The above analytical calculations demonstrate that the improved scheme for density gradient [i.e., Eq. (28)] is more accurate than the second-order ICS [i.e., Eq. (7)] when the density at the grid point is set to the analytical value. To numerically validate Eq. (28) and further compare Eqs. (28) with (7), the one-dimensional flat interface is simulated by the LB model with self-tuning EOS. The computational domain is chosen as $1024\delta_x \times 4\delta_x$ with the lattice spacing $\delta_x = 1$, and periodic boundary conditions are applied in both the x and y

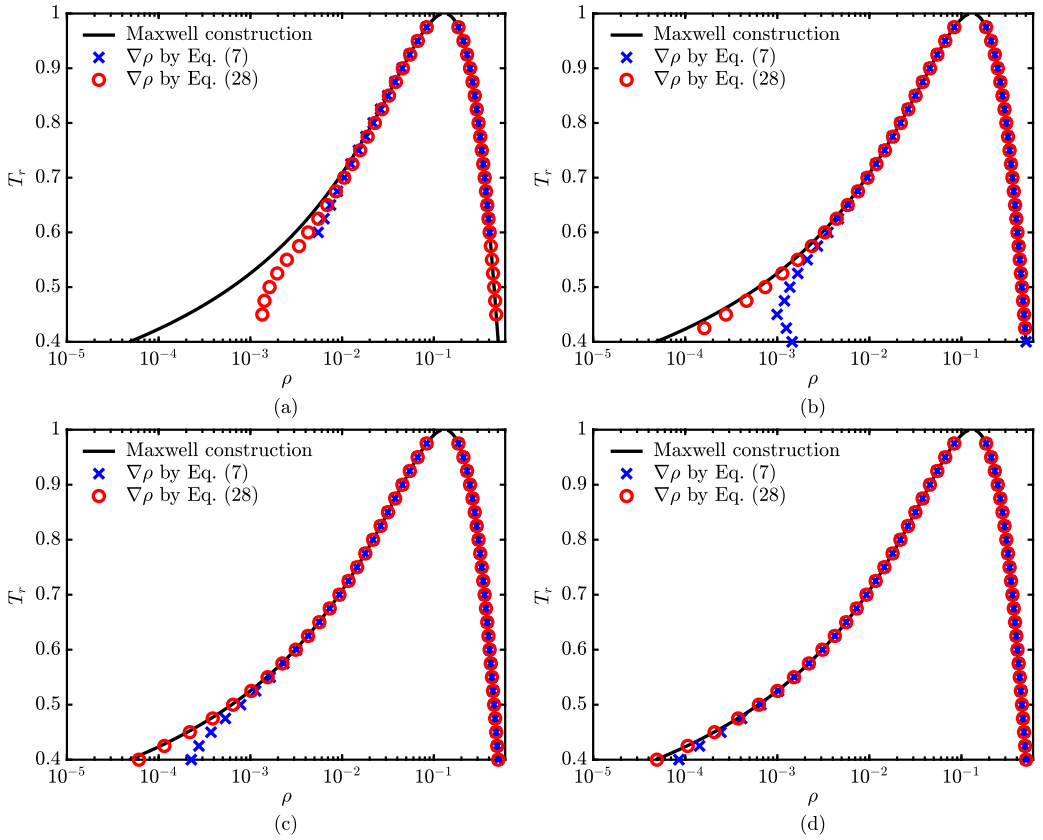

FIG. 4. Coexistence curves obtained by the simulations of one-dimensional flat interface with different schemes for $\nabla\rho$ and given by the Maxwell construction in thermodynamic theory. The surface tension is fixed at $\sigma = 0.01$ and the interface thickness is set to (a) $W = 5\delta_x$, (b) $W = 10\delta_x$, (c) $W = 20\delta_x$, and (d) $W = 40\delta_x$, respectively.

directions. At time $t = 0$, the density and velocity fields are initialized as

$$\rho(\mathbf{x}, 0) = \frac{\rho_{g,\text{Maxwell}} + \rho_{l,\text{Maxwell}}}{2} + \frac{\rho_{g,\text{Maxwell}} - \rho_{l,\text{Maxwell}}}{2} \times \tanh \frac{|x - x_c| - d_0/2}{W/\ln(19)}, \tag{35a}$$

$$\mathbf{u}(\mathbf{x}, 0) = \mathbf{0}, \tag{35b}$$

where $\rho_{g,\text{Maxwell}}$ and $\rho_{l,\text{Maxwell}}$ are the coexistence gas and liquid densities given by Maxwell construction, $x_c = 512\delta_x$ and $d_0 = 512\delta_x$ are the central position and initial width of the liquid phase, and W is the interface thickness. In the simulations, the dimensionless relaxation time τ ($\tau \equiv s_p^{-1}$) is chosen as 1.5 and the other relaxation parameters in $\mathbf{S}$ are set following Ref. [20]. The surface tension σ is fixed at 0.01 and the interface thickness W is set to $5\delta_x$, $10\delta_x$, $20\delta_x$, and $40\delta_x$, respectively. Figure 4 gives the coexistence curves obtained by the simulations with different schemes for density gradient. For comparison, the thermodynamic coexistence curve given by Maxwell construction is also plotted in Fig. 4. It can be seen that the coexistence curve with $\nabla\rho$ calculated by Eq. (28) agrees better with the thermodynamic curve than the one with $\nabla\rho$ calculated by Eq. (7) when the reduced temperature T_r is relatively low. In the situation with very small interface thickness ($W = 5\delta_x$), the simulation with Eq. (28) is more stable with respect to T_r than the simulation with Eq. (7). However, in the situation with $W = 10\delta_x$, the simulation with Eq. (7) becomes a little more stable, which is probably caused by the relatively large gas density that leads to a lower density ratio, as shown in Fig. 4(b). From Fig. 4, we can also see that the coexistence curve by simulation converges to the thermodynamic result as the interface thickness increases. This feature indicates that, for the LB model with self-tuning EOS, the deviation in gas branch is caused by the spatial discretization error in interfacial region and can be systematically reduced by grid refinement.

To further compare the numerical results obtained with $\nabla\rho$ by Eqs. (7) and (28), the relative error of gas density, defined as $E_{\rho,\text{gas}} = (\rho_{g,\text{numerical}} - \rho_{g,\text{Maxwell}})/\rho_{g,\text{Maxwell}}$, is computed here, and the variation of $E_{\rho,\text{gas}}$ with the reduced temperature T_r is given in Fig. 5. In a relatively low T_r range ($T_r \leqslant 0.675$) with a corresponding larger density ratio, $E_{\rho,\text{gas}}$ with $\nabla\rho$ by Eq. (28) is significantly smaller than $E_{\rho,\text{gas}}$ with $\nabla\rho$ by Eq. (7), and the gap tends to become larger as T_r decreases. However, in a relatively large T_r range ($T_r \geqslant 0.700$) with a corresponding lower density ratio, $E_{\rho,\text{gas}}$ with $\nabla\rho$ by Eq. (28) becomes a little larger than $E_{\rho,\text{gas}}$ with $\nabla\rho$ by Eq. (7), which is unexpected and may be explained as follows. For the simulation with Eq. (28), $E_{\rho,\text{gas}}$ is always larger than 0 and monotonically increases as T_r decreases. As for the simulation with Eq. (7), $E_{\rho,\text{gas}}$ is larger than 0 in the $T_r \leqslant 0.800$ range but becomes slightly smaller than 0 in the $T_r \geqslant 0.825$ range, which indicates that there exists a point with $E_{\rho,\text{gas}} = 0$ in the $0.800 < T_r < 0.825$ range. By further considering $E_{\rho,\text{gas}}$ tends to 0 as T_r tends to 1, the simulation with Eq. (7) could be

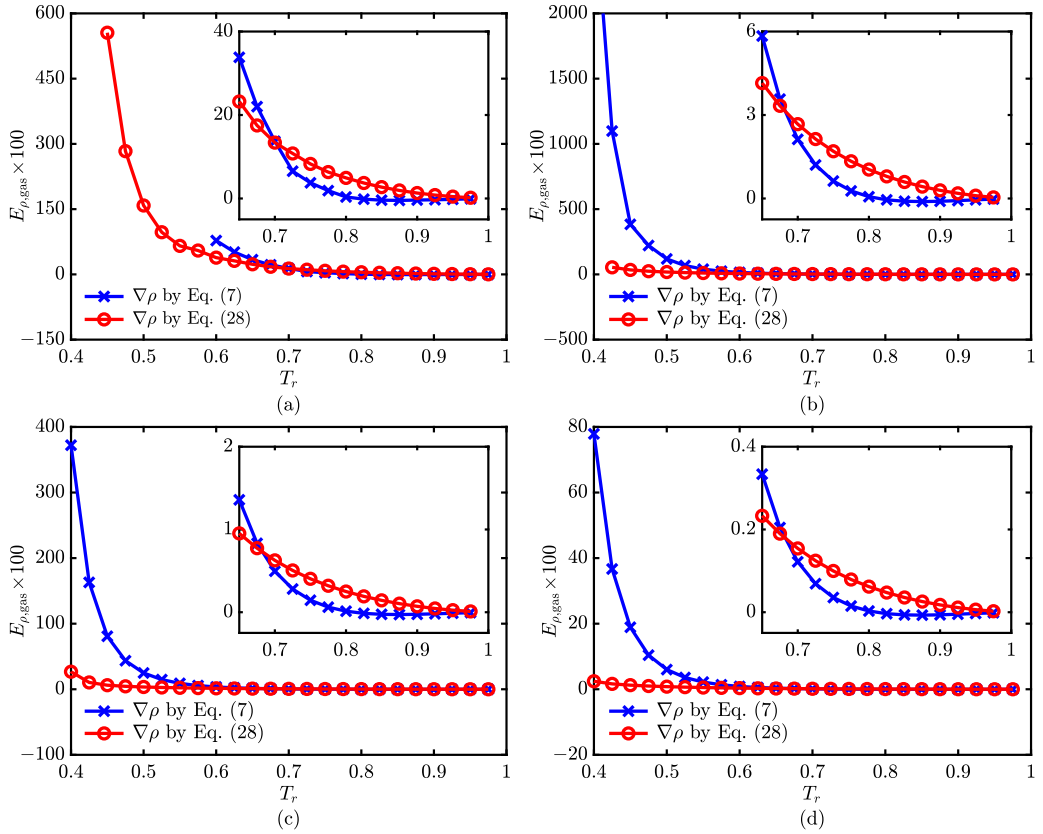

FIG. 5. Relative errors of gas density $E_{\rho,\mathrm{gas}} = (\rho_{g,\mathrm{numerical}} - \rho_{g,\mathrm{Maxwell}})/\rho_{g,\mathrm{Maxwell}}$ obtained by the simulations of one-dimensional flat interface with different schemes for $\nabla\rho$. The surface tension is fixed at $\sigma = 0.01$ and the interface thickness is set to (a) $W = 5\delta_x$, (b) $W = 10\delta_x$, (c) $W = 20\delta_x$, and (d) $W = 40\delta_x$, respectively.

relatively accurate in the $T_r \geqslant 0.700$ range. Nevertheless, the present improved scheme for density gradient [i.e., Eq. (28)] can help to achieve higher numerical accuracy when T_r is relatively low. Here, it is also worth pointing out that the simulation with Eq. (28) is actually acceptable in a relatively large T_r range because $E_{\rho,\mathrm{gas}}$ itself is quite small in this range due to the corresponding low density ratio, as clearly shown in Fig. 5.

B. Two-dimensional circular interface

To further validate the improved scheme for density gradient, a two-dimensional circular interface is considered in this part. In the equilibrium state, the chemical potential μ should be the same in the gas and liquid phases [41]. Thus, for a small variation in the interface radius r, there has

$$d\mu_g = d\mu_l, \tag{36}$$

where the subscripts "g" and "l" denote the gas and liquid phases, respectively. From Eq. (36) and considering an isothermal system, we have

$$\frac{1}{\rho_g} dp_g = \frac{1}{\rho_l} dp_l. \tag{37}$$

In addition, for the *two-dimensional* circular interface, the force balance equation (i.e., the Laplace law) can be written as

$$dp_l - dp_g = \sigma d\frac{1}{r}, \tag{38}$$

where σ is the surface tension. Note that $r > 0$ and $r < 0$ represent a droplet in gas phase and a bubble in liquid phase, respectively, and $r \to \infty$ indicates that the circular interface degenerates into a flat interface. From Eqs. (37) and (38), the densities (ρ_g and ρ_l) and pressures (p_g and p_l), as functions of the interface radius r, can be thermodynamically determined.

In practical applications, it would be difficult to solve Eqs. (37) and (38) because of the complexity of the EOS for multiphase fluids. Since the variations in densities (ρ_g and ρ_l) and pressures (p_g and p_l) caused by the circular interface are quite small, the nonlinear EOS can be locally linearized around the gas and liquid points, as illustrated by Fig. 6. Therefore, we have

$$dp_g = \varphi_{g,\mathrm{sat}} d\rho_g, \quad dp_l = \varphi_{l,\mathrm{sat}} d\rho_l, \tag{39}$$

where

$$\varphi_{g,\mathrm{sat}} \equiv \left.\frac{dp_{\mathrm{EOS}}}{d\rho}\right|_{\rho=\rho_{g,\mathrm{sat}}}, \quad \varphi_{l,\mathrm{sat}} \equiv \left.\frac{dp_{\mathrm{EOS}}}{d\rho}\right|_{\rho=\rho_{l,\mathrm{sat}}}. \tag{40}$$

Here, the subscript "sat" denotes the saturated state for flat interface. Using Eq. (39), Eqs. (37) and (38) can be easily

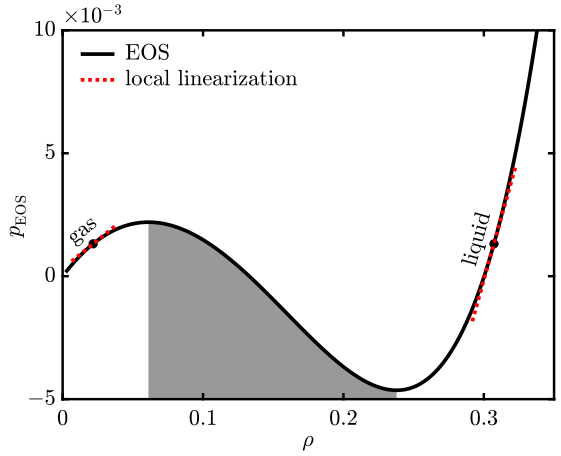

FIG. 6. Local linearization of the nonlinear EOS for multiphase fluids around the gas and liquid points. The density range with $\frac{dp_{\rm EOS}}{d\rho} < 0$ is depicted by the gray area.

integrated from a flat interface to a circular interface with radius r as follows:

$$\varphi_{g,\rm sat} \ln \frac{\rho_g}{\rho_{g,\rm sat}} = \varphi_{l,\rm sat} \ln \frac{\rho_l}{\rho_{l,\rm sat}}, \tag{41a}$$

$$\varphi_{l,\rm sat}(\rho_l - \rho_{l,\rm sat}) - \varphi_{g,\rm sat}(\rho_g - \rho_{g,\rm sat}) = \frac{\sigma}{r}, \tag{41b}$$

from which the gas and liquid densities can be easily determined. Here, it is worth pointing out that, if the liquid phase is incompressible (i.e., $\rho_l/\rho_{l,\rm sat} \to 1$) and the gas phase obeys the ideal-gas EOS (i.e., $p_g = K_{\rm EOS}\rho_g R_g T$), and if the liquid density is much larger than the gas density (i.e., $\rho_l \gg \rho_g$), Eq. (41) will degenerate into the Kelvin equation for gas pressure in thermodynamic theory [41].

The two-dimensional circular interface is simulated by the LB model with self-tuning EOS on a periodic domain with size being $1024\delta_x \times 1024\delta_x$. The interface thickness W and surface tension σ are fixed at $10\delta_x$ and 0.01, respectively, and the reduced temperature T_r is set to 0.7 and 0.6, respectively. The other parameters remain the same as those for the one-dimensional flat interface. In the simulations, the density and velocity fields are initialized as

$$\rho(\mathbf{x}, 0) = \frac{\rho_{g,\rm Maxwell} + \rho_{l,\rm Maxwell}}{2} + \frac{\rho_{g,\rm Maxwell} - \rho_{l,\rm Maxwell}}{2} \times \tanh \frac{|\mathbf{x} - \mathbf{x}_c|\mathrm{sgn}(r_0) - r_0}{W/\ln(19)}, \tag{42a}$$

$$\mathbf{u}(\mathbf{x}, 0) = \mathbf{0}, \tag{42b}$$

where r_0 is the initial radius and $\mathbf{x}_c$ is the central position of the computational domain. Fig. 7 shows the variation of the gas density ρ_g with the interface curvature $1/r$, where the analytical curve is determined by Eq. (41) and the equilibrium radius r in the simulation is measured at $\rho = (\rho_g + \rho_l)/2$ after convergence. It can be seen that for the case with $T_r = 0.7$, ρ_g with $\nabla\rho$ by Eq. (7) is in better agreement with the analytical curve than ρ_g with $\nabla\rho$ by Eq. (28). However, for the case with $T_r = 0.6$, ρ_g with $\nabla\rho$ by Eq. (28) becomes more accurate than ρ_g with $\nabla\rho$ by Eq. (7). Obviously, these results for the two-dimensional circular interface are fully consistent with the results in Fig. 5 for the one-dimensional flat interface. Therefore, the improved scheme for density gradient [i.e., Eq. (28)] is beneficial to the numerical accuracy when the reduced temperature is relatively low. From Fig. 7, it is also interesting to note that as compared with Eq. (7), the slope of the curve with $\nabla\rho$ by Eq. (28) agrees much better with the analytical curve for both $T_r = 0.7$ and $T_r = 0.6$.

Finally, a moving droplet in gas phase is simulated to further demonstrate the improved performance of Eq. (28). The simulation parameters remain the same as those for the foregoing stationary situation. As for the initial state, the density field is set to the convergent density field of the corresponding stationary situation with $r_0 = 128\delta_x$, and the velocity field is prescribed as $\mathbf{u}_0 \equiv (U_0, 0)^{\rm T}$. Here, it is worth pointing out that the elimination of the additional cubic terms of velocity is plugged into the LB model with self-tuning EOS for simulating the dynamic multiphase flows [20,34]. In the simulation, the total kinetic energy, defined as $E_k = \frac{1}{2}\int \rho\,|\mathbf{u} - \mathbf{u}_0|^2 d\mathbf{x}$, is computed. Fig. 8 shows the evolution of the total kinetic energy E_k with the time-step number t/δ_t. At $t/\delta_t = 0$, there has $E_k = 0$. When the quasi-steady state

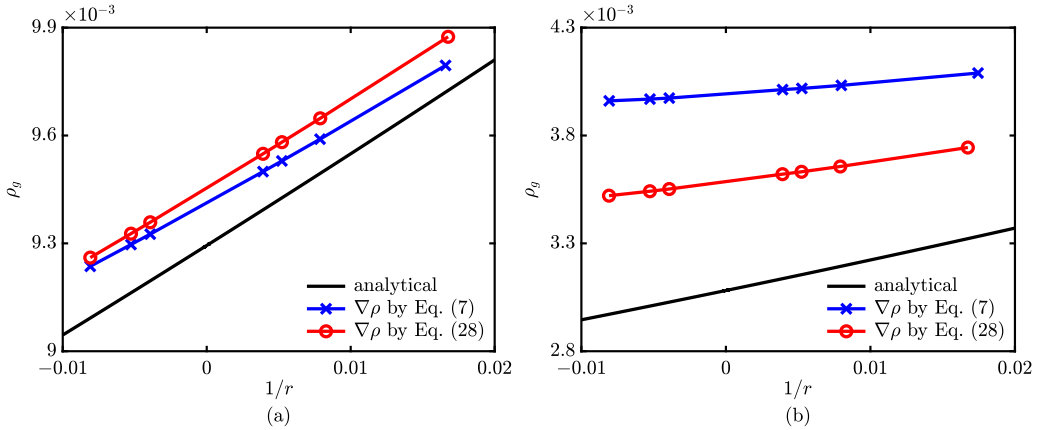

FIG. 7. Variations of the gas density ρ_g with the interface curvature $1/r$ obtained by the simulations of two-dimensional circular interface with different schemes for $\nabla\rho$ and analytically determined by Eq. (41). The interface thickness and surface tension are fixed at $W = 10\delta_x$ and $\sigma = 0.01$, respectively, and the reduced temperature is set to (a) $T_r = 0.7$ and (b) $T_r = 0.6$, respectively.

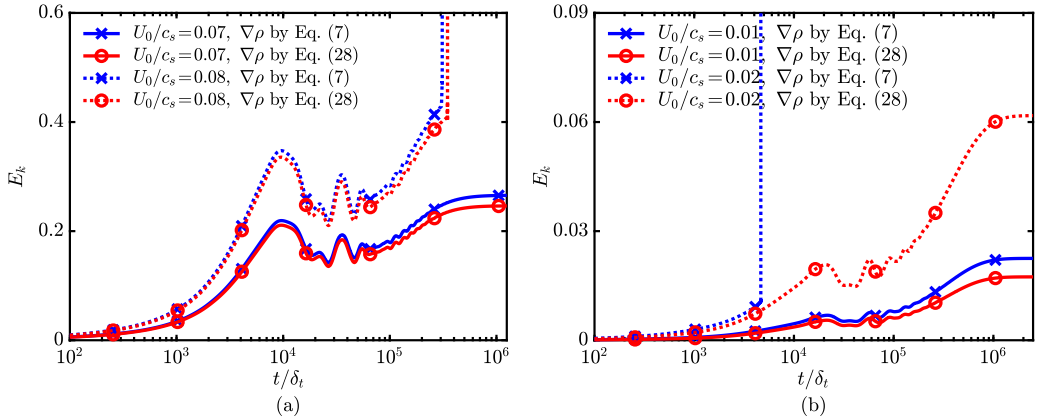

FIG. 8. Evolutions of the total kinetic energy E_k with the time-step number t/δ_t in the simulations of a moving droplet with different schemes for $\nabla\rho$ and different moving velocities. The initial radius, interface thickness, and surface tension are fixed at $r_0 = 128\delta_x$, $W = 10\delta_x$, and $\sigma = 0.01$, respectively, and the reduced temperature is set to (a) $T_r = 0.7$ and (b) $T_r = 0.6$, respectively.

is reached, both the velocities in liquid and gas phases will deviate from the prescribed velocity $\mathbf{u}_0$ [34], resulting in a finite value of E_k. From Fig. 8, the improved performance of Eq. (28) can be clearly seen. To be specific, E_k with $\nabla\rho$ by Eq. (28) is smaller than E_k with $\nabla\rho$ by Eq. (7) for both $T_r = 0.7$ and $T_r = 0.6$ as long as the simulations are stable. In addition, for the case with $T_r = 0.6$ and $U_0/c_s = 0.02$, the simulation with $\nabla\rho$ by Eq. (28) is stable, while the simulation with $\nabla\rho$ by Eq. (7) blows up after 4600 time steps.

V. CONCLUSION

In this work, the multiphase LB models based on pairwise interactions are theoretically analyzed in a unified framework. It is found that the gradient of density (or effective density, i.e., pseudopotential) is generally involved in this class of multiphase LB models and usually calculated by the second-order ICS simplified with the pairwise interaction force. Numerical tests show that the pairwise interaction force incorporated by the standard forcing scheme is quite accurate due to its explicit physical significance. The ε^3-order term, in which the density gradient is involved, should be viewed as a numerical trick and it is a major source of numerical error. Because of its thermodynamic consistency, the recent multiphase LB model with self-tuning EOS is focused on, and an improved scheme is then proposed on the basis of a low Mach number approximation to calculate the density gradient for this model. Analytical calculations demonstrate that the present improved scheme is more accurate than the previous second-order ICS. Numerical simulations show that the results obtained with the improved scheme are in better agreement with the thermodynamic results when the reduced temperature is relatively low.

ACKNOWLEDGMENTS

R.H. acknowledges the support by the Alexander von Humboldt Foundation, Germany. This work was also supported by the National Natural Science Foundation of China through Grants No. 51820105009 and No. 51536005.

[1] A. Fazeli, S. Bigham, and S. Moghaddam, Int. J. Heat Mass Transf. **95**, 368 (2016).
[2] K. Choi, A. H. C. Ng, R. Fobel, and A. R. Wheeler, Annu. Rev. Anal. Chem. **5**, 413 (2012).
[3] X. He and G. D. Doolen, J. Stat. Phys. **107**, 309 (2002).
[4] G. R. McNamara and G. Zanetti, Phys. Rev. Lett. **61**, 2332 (1988).
[5] X. He and L.-S. Luo, Phys. Rev. E **55**, R6333 (1997).
[6] X. Shan, X.-F. Yuan, and H. Chen, J. Fluid Mech. **550**, 413 (2006).
[7] A. K. Gunstensen, D. H. Rothman, S. Zaleski, and G. Zanetti, Phys. Rev. A **43**, 4320 (1991).
[8] X. Shan and H. Chen, Phys. Rev. E **47**, 1815 (1993).
[9] M. R. Swift, W. R. Osborn, and J. M. Yeomans, Phys. Rev. Lett. **75**, 830 (1995).
[10] X. He, X. Shan, and G. D. Doolen, Phys. Rev. E **57**, R13 (1998).
[11] D. Grunau, S. Chen, and K. Eggert, Phys. Fluids A **5**, 2557 (1993).
[12] X. Shan and H. Chen, Phys. Rev. E **49**, 2941 (1994).
[13] M. R. Swift, E. Orlandini, W. R. Osborn, and J. M. Yeomans, Phys. Rev. E **54**, 5041 (1996).
[14] X. He, S. Chen, and R. Zhang, J. Comput. Phys. **152**, 642 (1999).
[15] T. Inamuro, T. Ogata, S. Tajima, and N. Konishi, J. Comput. Phys. **198**, 628 (2004).
[16] X. Frank, P. Perré, and H. Z. Li, Phys. Rev. E **91**, 052405 (2015).
[17] M. Sbragaglia, K. Sugiyama, and L. Biferale, J. Fluid Mech. **614**, 471 (2008).
[18] Q. Li, K. H. Luo, Q. J. Kang, Y. L. He, Q. Chen, and Q. Liu, Prog. Energy Combust. Sci. **52**, 62 (2016).
[19] L.-S. Luo, Phys. Rev. Lett. **81**, 1618 (1998).

[20] R. Huang, H. Wu, and N. A. Adams, Phys. Rev. E **99**, 023303 (2019).
[21] A. L. Kupershtokh, in *Proceedings of the 5th International EHD Workshop* (University of Poitiers, Poitiers, France, 2004), pp. 241–246.
[22] A. L. Kupershtokh, D. A. Medvedev, and D. I. Karpov, Comput. Math. Appl. **58**, 965 (2009).
[23] H. Huang, M. Krafczyk, and X. Lu, Phys. Rev. E **84**, 046710 (2011).
[24] Q. Li, K. H. Luo, and X. J. Li, Phys. Rev. E **86**, 016709 (2012).
[25] X. Shan, Phys. Rev. E **77**, 066702 (2008).
[26] Q. Li, K. H. Luo, and X. J. Li, Phys. Rev. E **87**, 053301 (2013).
[27] D. Lycett-Brown and K. H. Luo, Phys. Rev. E **91**, 023305 (2015).
[28] D. Lycett-Brown and K. H. Luo, Phys. Rev. E **94**, 053313 (2016).
[29] R. Huang and H. Wu, J. Comput. Phys. **327**, 121 (2016).
[30] M. E. McCracken and J. Abraham, Phys. Rev. E **71**, 036701 (2005).
[31] P. Lallemand and L.-S. Luo, Phys. Rev. E **61**, 6546 (2000).
[32] Y. H. Qian, D. d'Humières, and P. Lallemand, Europhys. Lett. **17**, 479 (1992).
[33] Z. Guo, C. Zheng, and B. Shi, Phys. Rev. E **65**, 046308 (2002).
[34] R. Huang, H. Wu, and N. A. Adams, Phys. Rev. E **97**, 053308 (2018).
[35] P. J. Dellar, J. Comput. Phys. **259**, 270 (2014).
[36] R. Huang, H. Wu, and N. A. Adams, J. Comput. Phys. **392**, 227 (2019).
[37] X. Shan, Phys. Rev. E **73**, 047701 (2006).
[38] Q. Li, P. Zhou, and H. J. Yan, Phys. Rev. E **94**, 043313 (2016).
[39] H. Paillere, C. Viozat, A. Kumbaro, and I. Toumi, Heat Mass Transf. **36**, 567 (2000).
[40] N. F. Carnahan and K. E. Starling, J. Chem. Phys. **51**, 635 (1969).
[41] J. S. Rowlinson and B. Widom, *Molecular Theory of Capillarity* (Oxford University Press, Oxford, 1982).